Spectroscopic analysis of vibronic relaxation pathways in molecular spin qubit $[Ho(W_5O_{18})_2]^{9-}$: sparse spectra are key

Avery L. Blockmon,[†,‡] Aman Ullah,[†,¶] Kendall D. Hughey,[‡] Yan Duan,[¶] Kenneth R. O'Neal,[‡] Mykhaylo Ozerov,[§] José J. Baldoví,[¶] Juan Aragó,[¶] Alejandro Gaita-Ariño,[*,¶] Eugenio Coronado,[¶] and Janice L. Musfeldt[*,‡,∥]

[†]These authors contributed equally to this work

[‡]Department of Chemistry, University of Tennessee, Knoxville, Tennessee 37996, USA

[¶]Instituto de Ciencia Molecular, Universitat de Valencia, Paterna 46980, Spain

[§]National High Magnetic Field Laboratory, Tallahassee, Florida, 32310, USA

[∥]Department of Physics, University of Tennessee, Knoxville, Tennessee 37996, USA

E-mail: gaita@uv.es; musfeldt@utk.edu

Abstract

Vibrations play a prominent role in magnetic relaxation processes of molecular spin qubits as they couple to spin states, leading to the loss of quantum information. Direct experimental determination of vibronic coupling is crucial to understand and control the spin dynamics of these nano-objects, which represent the limit of miniaturization for quantum devices. Herein, we measure the magneto-infrared properties of the molecular spin qubit system $Na_9[Ho(W_5O_{18})_2]\cdot35H_2O$. Our results place significant constraints on the pattern of crystal field levels and the vibrational excitations allowing us to unravel vibronic decoherence pathways in this system. We observe field-induced spectral

1

changes near 63 and 370 cm^{-1} that are modeled in terms of odd-symmetry vibrations mixed with f-manifold crystal field excitations. The overall extent of vibronic coupling in Na$_9$[Ho(W$_5$O$_{18}$)$_2$]·35H$_2$O is limited by a modest coupling constant (on the order of 0.25) and a transparency window in the phonon density of states that acts to keep the intramolecular vibrations and M_J levels apart. These findings advance the understanding of vibronic coupling in a molecular magnet with atomic clock transitions and suggest strategies for designing molecular spin qubits with improved coherence lifetimes.

KEYWORDS: mononuclear lanthanide complexes, atomic clock transitions, relaxation pathways, magneto-infrared spectroscopy, single molecule magnets, molecular spin qubits, vibronic coupling, polyoxometalates

Introduction

Quantum two-level systems based on spin states known as "spin qubits" are promising building blocks for the development of quantum technologies. In contrast with classical bits that are defined by two states "0" or "1", qubits exploit quantum behavior by allowing superposition between the basis states. Among different physical platforms, chemistry contributes to this effort via the study of spin states in magnetic molecules, both in the form of molecular spin qubits and molecular nanomagnets. In this context, mononuclear lanthanide complexes provide ideal settings that represent the limit of miniaturization for quantum and classical magnetic memories, respectively.[1-3]

Hundreds of such systems have been characterized so far in an attempt to understand and control their physical properties.[4-6] A judicious chemical design exploiting magnetic anisotropy and optimizing the molecular structure versus spin-vibrational coupling led to the observation of magnetic bistability up to 80 K and an effective energy barrier of 2217 K in the molecular nanomagnet [(Cp^{iPr5})Dy(Cp*)]$^+$.[7] Regarding molecular spin qubits, prominent examples include: two vanadium(IV) complexes, namely (i) [V(C$_8$S$_8$)$_3$]$^{2-}$, which shows a record

phase memory time T_M of 0.7 ms[8] and (ii) VOPc, with coherence times up to 1 μs at room temperature;[9] (iii) a Cu^{2+} complex, $[P(Ph_4)]_2[Cu(mnt_2)]$ (mnt^{2-}=maleonitriledithiolate), that preserves coherence up to room temperature[10] when diluted in Ni^{2+}; and (iv) a Ln^{3+}-based molecular nanomagnet, $[Ho(W_5O_{18})_2]^{9-}$, whose spin qubit dynamics are protected against magnetic noise at optimal operating points known as atomic clock transitions.[11] In this work, we focus on $Na_9[Ho(W_5O_{18})_2]\cdot35H_2O$, investigating the specific vibronic relaxation pathways[12–15] that govern magnetic relaxation. Thus far, the T_1 (spin-lattice relaxation time) pathways that determine T_2 (the transverse relaxation time due to both spin-spin and phonon scattering) are largely under-explored - not just in this system but in molecular spin qubits in general.[16,17] In particular, while transitions between electron-nuclear spin states are protected from quantum decoherence at the atomic clock transitions, this protection of the quantum information is only from magnetic noise. Indeed, the system suffers from a 50% reduction of the T_2 relaxation time between 5 and 7 K due to thermal noise, which limits coherence.[11] This thermal dependence is intriguing in the sense that it cannot be explained by Orbach processes. At very low temperatures and magnetic fields away from the clock transitions, the main source of decoherence will be dipole-dipole interactions.

Single molecule magnet behavior in $Na_9[Ho(W_5O_{18})_2]\cdot35H_2O$ arises from the magnetic anisotropy of a Ho^{3+} ion ($J = 8$) encapsulated by two polyoxometalate moieties in an eight-fold oxygen coordination environment with local slightly distorted D_{4d} symmetry (Fig. 1).[18–20] This assignment stabilizes an $M_J = \pm4$ ground state. In the crystal, the $[Ho(W_5O_{18})_2]^{9-}$ anions are held together by interactions with Na^+ ions and free water molecules of crystallization with a space group $P\bar{1}$.[21] The magnetic properties of $Na_9[Ho(W_5O_{18})_2]\cdot35H_2O$ have attracted significant attention. The out-of-phase ac magnetic susceptibility displays a maximum near 5 K over the 10^3 - 10^4 Hz range,[19] and magnetization shows a slow relaxation[19] - a key signatures of single molecule magnetism.[22] Electron paramagnetic resonance sports an eight line spectrum due to the ground M_J level hyperfine coupling to the $I = 7/2$ nuclear spin along with a tunneling gap of approximately 9 GHz (0.3 cm^{-1}).[23] Two-pulse electron

spin echo measurements at its optimal working points reveal spin coherence times up to T_2 = 8.4 μs at 5 K when diluted to a 1% concentration in the isostructural diamagnetic matrix of its Y^{3+}-based analog $Na_9[Ho_{0.01}Y_{0.99}(W_5O_{18})_2]\cdot35H_2O$. The high dilution limit for T_2 in other molecular spin qubits is usually achieved at concentrations around 0.01%.[11] Recent results operating at these special points reveal the possibility of quantum magnetoelectric coupling, where voltage control of the crystal field levels can be used to manipulate the spin qubit states.[24]
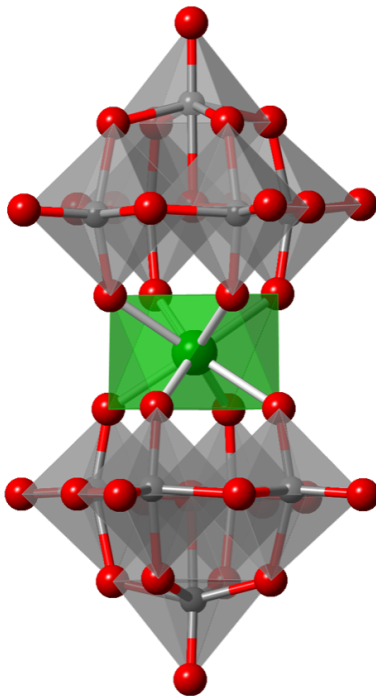

Figure 1: Structure of the molecular anion $[Ho(W_5O_{18})_2]^{9-}$. Color code: Ho (green), W (gray) and O (red).

Despite the importance of the crystal field levels in this system, spectroscopic information is limited to the aforementioned 0.3 cm^{-1} tunneling splitting in the ground doublet determined by electron paramagnetic resonance as well as the low energy M_J levels at 41 and 49 cm^{-1} measured by inelastic neutron scattering by Vonci *et. al.*[25] A number of authors have attempted to locate the position and determine the order of the rest of the crystal field energy levels in $Na_9[Ho(W_5O_{18})_2]\cdot35H_2O$.[25,26] While it is very much accepted that the seventeen different M_J levels reside between 0.3 and 400 cm^{-1},[25,26] the exact pattern and

order has been elusive due to the anisotropy of the system along with coupling to the vibrational levels.[25] Moreover, Ho^{3+} is a non-Kramers ion, so while at first glance, it appears that many of the crystal field levels are doubly-degenerate, there is a very small energy scale that splits the M_J levels and relieves their apparent degeneracies.[25] Although there is some prior infrared spectroscopy,[19] the work focused only on the middle infrared and, as a result, did not explore excitations below 400 cm^{-1} which - based on energy scale arguments - are likely to interact with spin excitations, changes in spin state, and crystal field energy levels.[27,28] At the same time, the vibrational features in $Na_9[Ho(W_5O_{18})_2]\cdot35H_2O$ are unassigned,[19] making it difficult to test the order of the Ho^{3+} crystal field excitations or model coupling processes. This is important because, as a candidate qubit material, it is crucial to unravel all decoherence mechanisms that emanate from lossy responses in this frequency range.[29,30]

In order to explore the dynamics of a molecular magnet with atomic clock transitions, we combined far infrared spectroscopy and high magnetic field techniques with lattice dynamics calculations and vibronic coupling models to reveal the low energy excitations in $Na_9[Ho(W_5O_{18})_2]\cdot35H_2O$. Strong magneto-infrared effects are observed near 370 and 63 cm^{-1} due to vibrational transition intensities modulated by mixing with f-manifold crystal field excitations. These structures place significant constraints on the position of several M_J levels - including the highest energy set - establishing stringent bounds on the entire series of excitations. Our analysis suggests that coherence in $Na_9[Ho(W_5O_{18})_2]\cdot35H_2O$ benefits from the limited frequency overlap between crystal field levels and the phonon manifold. Moreover, we demonstrate that the limited frequency overlap is due to a transparency window or "hole" in the phonon density of states. This renders many of the M_J levels ineffective in terms of engaging in vibronic coupling. While the concept of spectral sparsity has been articulated in the past, the approach has been mainly qualitative. The significant conceptual advance in this work is that we specifically identify the mechanism of vibronic coupling in $Na_9[Ho(W_5O_{18})_2]\cdot35H_2O$ including how and why some interactions are active while others are blocked. These findings provide a strategy for the chemical design of molecular nanomag-

nets and spin qubits with a full separation of electronic and vibrational excitations. Such an approach has the potential to eliminate vibronic coupling as a decoherence mechanism.[31–34]

Results and discussion

Assigning the low energy excitations in $Na_9[Ho(W_5O_{18})_2]\cdot35H_2O$

Figure 2 summarizes the far infrared response of $Na_9[Ho(W_5O_{18})_2]\cdot35H_2O$. As a reminder, we focus our efforts on the low frequency regime from 25 - 600 cm^{-1} because (i) the far infrared contains key vibrations involving the Ho^{3+} center as well as crystal field levels, and (ii) the middle infrared was studied in prior work.[19] Figure 2 includes a number of important measurements, predictions, and simulations for comparison. Many of these excitations are vibrational in nature, and with the aid of our lattice dynamics calculations, we can assign the peaks and model the overall spectrum. For instance, we assign the dominant peak at 365 cm^{-1} as a rocking motion of HoO_4. This rocking motion is accompanied by minor distortions
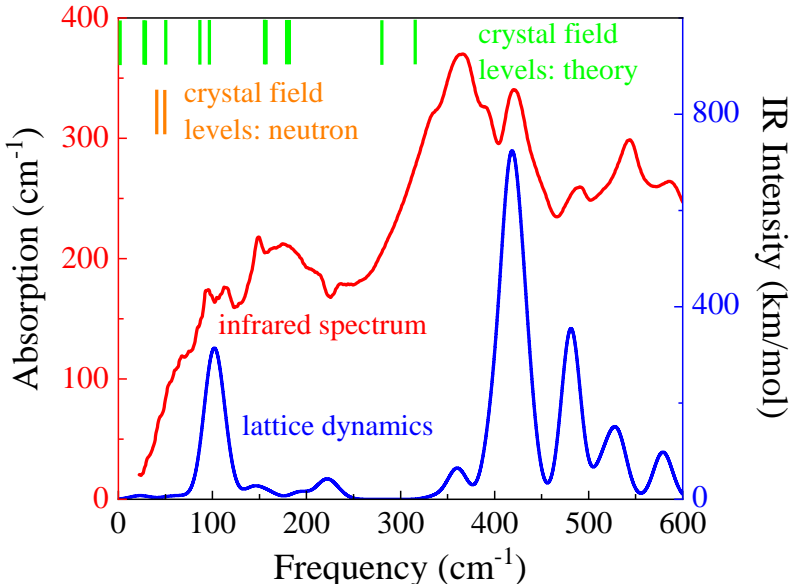

Figure 2: Far infrared spectrum of $Na_9[Ho(W_5O_{18})_2]\cdot35H_2O$ at room temperature compared with calculated lattice dynamics of the building block anion and calculated f-manifold crystal field levels with various M_J's. Neutron scattering data from Reference 25 is included as well.

of the $(W_5O_{18})^{6-}$ cages. The theoretically predicted vibrational response (appropriately broadened) is shown in blue for comparison. The overall agreement with the measured spectrum is reasonable. Interestingly, our lattice dynamics calculations reveal a broad range - from approximately 250 to 330 cm^{-1} - where the fundamental excitations of the lattice are missing. The absence of spectral features in this region is a consequence of a "hole" in the phonon density of states. While less apparent than in the theoretical response, there is wide minimum in the infrared spectrum in the same general vicinity. The implications of this structure will be discussed below. Complete vibrational mode assignments are available in Table S1 of the Supporting Information. The features listed in this table are primarily (but not exclusively) intramolecular vibrations. As a reminder, water-related vibrational modes resonate at higher frequencies; even the H_2O libration is above 450 cm^{-1}.[35,36]

f-block elements like Ho^{3+} also display crystal field levels in the far infrared.[37–39] The exact position of the f-manifold levels varies significantly depending upon the details of the crystal field environment.[15,40,41] Previous authors located the $M_J = \pm 3$ and ± 5 levels in $Na_9[Ho(W_5O_{18})_2]\cdot35H_2O$ via inelastic neutron scattering.[25] These energies are shown in Fig. 2 in orange and help to define a lower limit to the crystal field manifold. As part of this work, we computed the full set of Ho^{3+} crystal field levels for this system. They are included in Fig. 2 in green for comparison. Our predictions for the position of the $M_J = \pm3$ and ±5 levels are consistent with the neutron scattering results.[25] The upper M_J levels obtained from our model are also in close proximity to various molecular vibrations involving the central holmium atom and coordinated oxygen atoms. Hyperfine splitting of the Ho nuclear spin states is also consistent with the low temperature specific heat.[19]

Figure 3 shows the calculated crystal field levels in greater detail along with their evolution under magnetic field applied along the long molecular axis. The evolution for other directions of the magnetic field are shown in Fig. S7 of the Supporting Information. As expected, the Zeeman effect between 0 and 35 T widens the total spread of the crystal field levels, with each level acquiring a slope proportional to its expectation value $< M_J >$. The

slopes becoming non-linear as a result of either avoided crossings among crystal field levels or transverse magnetic fields.
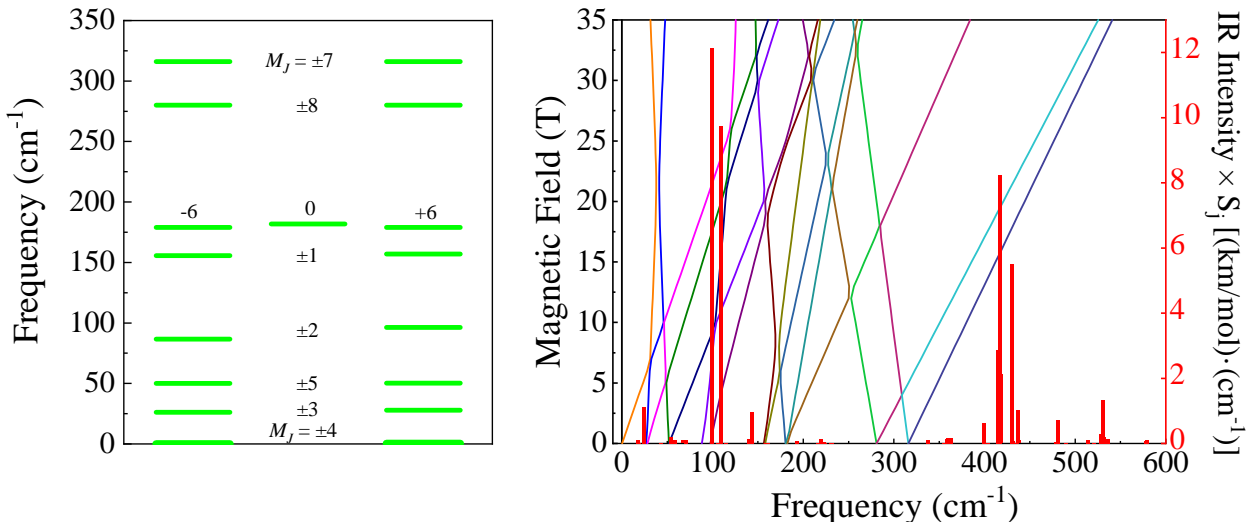

Figure 3: Left: Calculated crystal field levels of the $[\text{Ho}(\text{W}_5\text{O}_{18})_2]^{9-}$ cluster anion. Note that the energies are normalized to the ground M_J state. The $M_J = 0$ level is singly degenerate, and the others are all doubly degenerate. These M_J levels are also shown in Fig. 2 (along the top, in green). Right: Double y-axis plot of calculated crystal field levels as a function of magnetic field and vibrational mode intensities times the vibronic coupling coefficient (S_j).

We also measured the far infrared response of $\text{Na}_9[\text{Ho}(\text{W}_5\text{O}_{18})_2]\cdot35\text{H}_2\text{O}$ as a function of temperature. As shown in Fig. S2 of the Supporting Information, the lattice - as represented by these vibrational excitations - does not change significantly with temperature. These findings were verified by complementary measurements of the non-magnetic analog $\text{Na}_9[\text{Y}(\text{W}_5\text{O}_{18})_2]\cdot35\text{H}_2\text{O}$. Further, the Ho and Y analogs have identical transparency windows in the infrared response (Fig. S1 of the Supporting Information). The phonon density of states is therefore not radically different than in the diluted case represented by $\text{Na}_9[\text{Ho}_{0.01}\text{Y}_{0.99}(\text{W}_5\text{O}_{18})_2]\cdot35\text{H}_2\text{O}$.[11] Although there are uncoordinated waters in the crystal structure, the slight blue shifting of peaks demonstrates that hydrogen bonding does not strengthen significantly at low temperature.[42]

Magneto-infrared response of $Na_9[Ho(W_5O_{18})_2] \cdot 35H_2O$

Figure 4 (a,b) displays the magneto-infrared response of $Na_9[Ho(W_5O_{18})_2] \cdot 35H_2O$ at 4.2 K. The spectra are in the form of absorption differences, $\Delta\alpha(H) = \alpha(H) - \alpha(H = 0$ T$)$, which serve to highlight field-induced changes. The latter are not always apparent in the absolute absorption. There are two primary structures that develop systematically under applied field: (i) a set of sharp features centered near 63 cm^{-1}, and (ii) several broader, more complex structures between 335 and 400 cm^{-1}. Contour plots also show the development of the absorption differences with increasing magnetic field (Fig. 4 c,d). For comparison purposes, we performed similar measurements on the non-magnetic analog $Na_9[Y(W_5O_{18})_2] \cdot 35H_2O$. No field-induced spectral changes were observed - as anticipated.
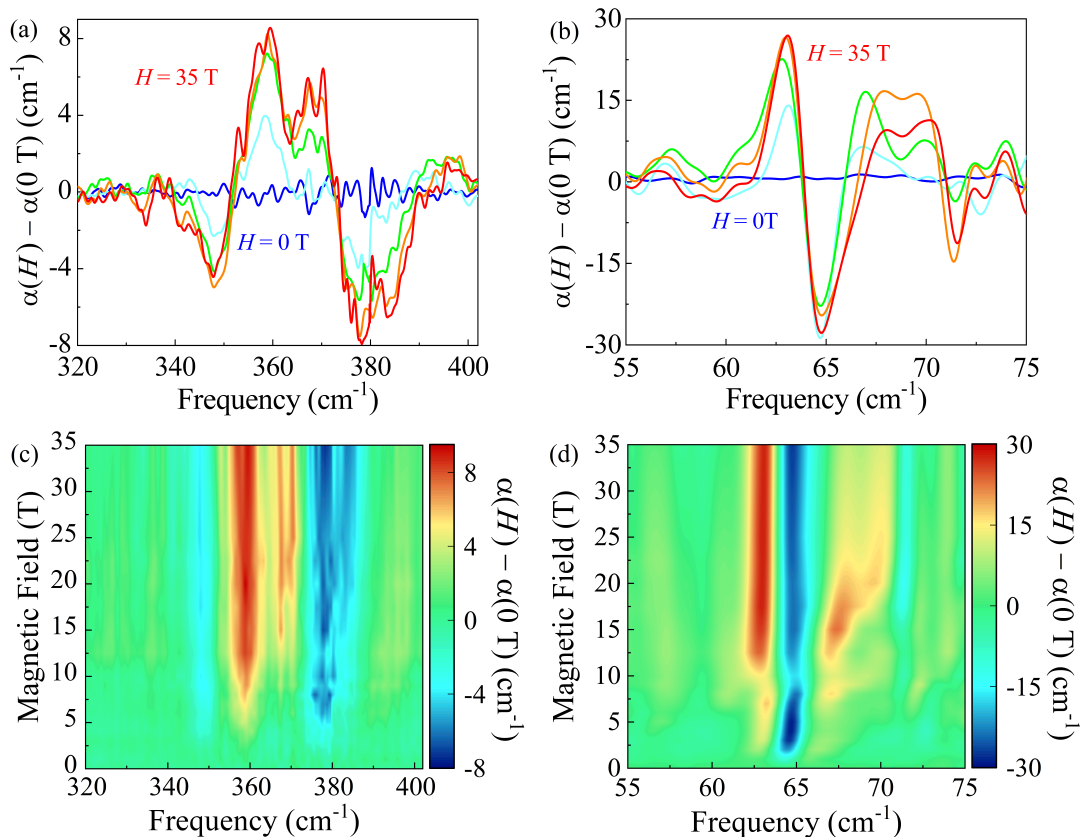

Figure 4: (a,b) Magneto-infrared response of the features centered at 370 and 63 cm^{-1}, respectively, at 0, 5, 12.5, 20 and 35 T. The data are shown as absorption differences: $\Delta\alpha(\omega, H) = \alpha(\omega, H) - \alpha(\omega, H = 0$ T$)$. (c,d) Contour plots of the absorption difference spectra from panels (a,b) over the full range of magnetic fields. Scale bars are included.

9

We assign contrast in the absorption difference spectra of $Na_9[Ho(W_5O_{18})_2]\cdot 35H_2O$ based upon the position of the intramolecular vibrations and f-manifold crystal field levels discussed in Fig. 2. The magneto-infrared features centered near 360 cm^{-1} are in close proximity to several different vibrational modes including HoO_8 rocking and stretching modes - all of which take place in the center of the cage. Therefore, at first glance, it may seem that the magneto-infrared response in this frequency region may be due to spin-lattice coupling. However, the lack of a change in the spin-spin correlation function argues against this interpretation.[43] Other candidate excitations include crystal field levels. The highest frequency set, $M_J = \pm 7$ are calculated by ourselves and others[25] to be in this vicinity. This suggests that vibronic coupling - in which the crystal field levels move with applied magnetic field and are mixed with (and affect the intensity of) nearby vibrational modes - may be responsible for the magneto-infrared contrast.[28,44,45] We test both models in this work and establish the vibronic coupling model below. Thus, the assignment of the $M_J = \pm 7$ levels interacting with nearby phonons serves as an upper bound for the entire f-manifold of Ho^{3+} excitations. This assignment is based upon our detailed calculations of the crystal field levels (Fig. 3). These crystal field levels shift with applied magnetic field and vibronically couple with appropriate vibrational modes while in their proximity. The maximum vibronic coupling that we calculate in our system is <0.25 cm^{-1} (Table S3, Supporting Information). This is the reason why the magneto-infrared response shows a relatively constant frequency with magnetic field while the intensity grows with field. We see a progressive saturation of the magneto-infrared response with increasing field up to 35 T (Fig. S4, Supporting Information). We expect that the magneto-infrared signature will decrease at even higher fields as the crystal field levels move away from the phonons with which they are mixed. Such a trend is observed in $Co[N(CN)_2]_2$.[28]

A similar mechanism can explain the contrast centered near 63 cm^{-1} (Fig. 4b). While our dynamics calculations predict significant intensity for localized vibrational modes starting at 100 cm^{-1} (Fig. 2), $Na_9[Ho(W_5O_{18})_2]\cdot 35H_2O$ has lattice modes involving asymmetric

stretching of the HoO_8 along with cage tilting in the same frequency range as well. While the details depend upon the precise environment and long-range crystallographic orientation of the polyoxometalates, these vibrations can act as symmetry-breakers for the large number of f-manifold excitations in the vicinity. Contrast centered near 63 cm^{-1} in the magneto-infrared spectra of $Na_9[Ho(W_5O_{18})_2]\cdot35H_2O$ is therefore attributed to odd-symmetry vibrational modes activating excitations involving nearby crystal field levels - specifically the M_J = ±5 levels. It is possible that the ±2 levels contribute as well.

To elucidate the origin of the magneto-infrared response, we simulated the absorption spectrum of this molecular nanomagnet at different fields. In absence of vibronic coupling, selection rules yield a trivial result that fails to reproduce the experimental behavior. Indeed this calculation results in the sum of purely vibrational features (with no field dependence) as shown in Fig. 2 along with a collection of field-dependent but strongly forbidden transitions among f-manifold crystal field levels. We instead employ a more realistic model to estimate the transition dipole matrix between all possible vibrational and crystal field levels. Crucially, this model considers vibronic eigenfunctions, allowing for mixing between the two kinds of excitations (Section S3, Supporting Information).

We simulated the magneto-infrared response of $Na_9[Ho(W_5O_{18})_2]\cdot35H_2O$ using this approach (Fig. 5). Examining the absorption difference spectra up to 35 T, we find consistent results, with two regions of notable effects at relatively low and high frequencies. There is a wide break in the absorption difference spectrum between 200 and 390 cm^{-1} devoid of any significant anti-crossings. Let us first discuss the high frequency region (emphasized on the right-hand side of Fig. 5), which corresponds to the most systematic set of experimental features. Here, the calculated absorption difference spectra evolve in a very simple manner, in good agreement with the experimental results. In particular, the calculations reproduce the gradual saturation of the absorption difference with increasing field (Fig. S4). The microscopic origin of this behavior is modelled as a field dependence of the vibronic wavefunctions (Section S3.3, Supporting Information), including representative vibronic wave functions and
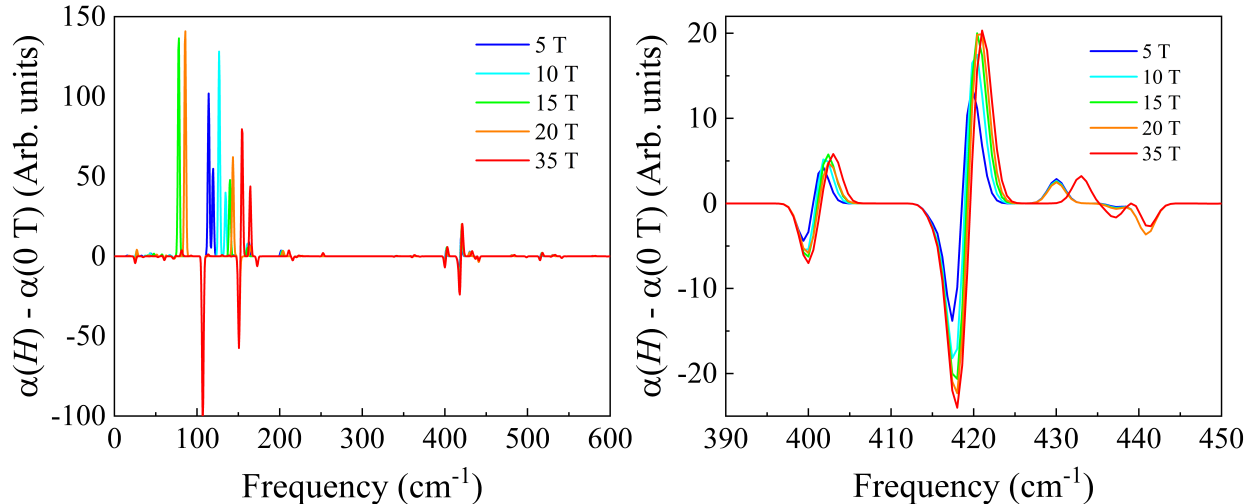
Figure 5: Left: Simulated magneto-infrared spectra of the building block anion $[Ho(W_5O_{18})_2]^{9-}$ between 5 and 35 T. The data are presented in the form of an absorption difference for easy comparison with Fig. 4 . Right: Close-up view of the calculated magneto-infrared response over the same field range.

energies at 0 T and 5 T to illustrate the manner in which the magnetic field modulates the wave function mixing. Overall the agreement is very satisfactory, save for a rigid 40 cm^{-1} blue shift from our experimental features. This frequency shift is attributed to performing calculations on the isolated molecular $[Ho(W_5O_{18})_2]^{9-}$ anion as compared to the entire environment in $Na_9[Ho(W_5O_{18})_2]\cdot35H_2O$. In the low frequency region (left-hand side of Fig. 5), the theoretically calculated features are similarly blue shifted. In addition, the behavior is more complex - both in our measurements and simulation. Part of the complexity may be due to the high density of M_J levels in this region blue which undergo significant anti-crossings (Fig. 3). These M_J levels interact with nearby phonons as they pass across various resonance frequencies, and this vibronic coupling interaction is observable in the both experimental and simulated magneto-infrared spectra.

Developing molecular design criteria to mitigate vibronic coupling

One strategy for the rational design of longer-lived molecular spins is decoupling spin energy levels from vibrational excitations. The effort is generally two-fold. First, one needs a

sparse low-energy crystal field spectrum. Such a manifold of energy levels can arise from a very strong crystal field as in dysprosocenium,[7] from the bunching of crystal field levels at higher frequencies as in Tb bis-phthalocyaninato sandwiches,[46] or from incorporating U as a magnetic center.[47] Altering the coordination environments can also displace the M_J levels to other regions of the spectra. Second, one needs an effectively sparse low frequency vibrational spectrum. This can result from a molecular environment that is either very simple, like in small molecules with fewer degrees of freedom,[8,10] or very rigid systems, such as fully aromatic ligands,[9] where vibrations are pushed to higher frequency or engage in exceptionally limited vibronic coupling. The point is that by placing these features off-resonance, thermal routes to decoherence may be weakened and potentially curtailed. Another method of separating the spin energy levels from vibrational excitations is by isotropic substitution. Use of heavier isotopes such as ^{18}O rather than ^{16}O obviously reduces mode frequencies and shifts the position of the transparency window (Fig. 6). One could use this method to move vibrational modes away from nearby M_J levels as well. Pressure or strain might be an even more effective strategy for moving the phonon resonances out of the way.
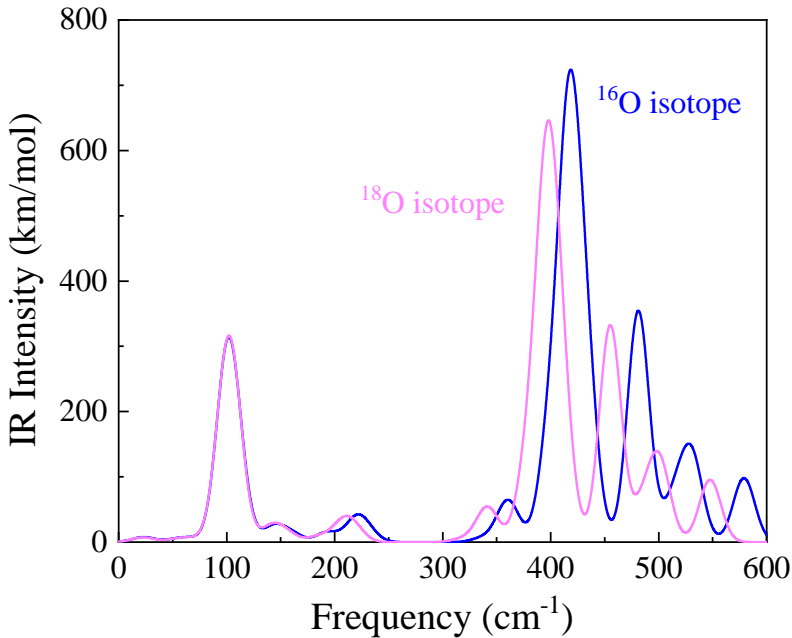

Figure 6: Calculated lattice dynamics spectra of $[Ho(W_5O_{18})_2]^{9-}$ with different isotopes of oxygen. ^{18}O substitution decreases T_1 slightly - on the order of 1%.

13

In terms of the electronic spectrum, polyoxometalates offer the key advantage of maintaining a very similar coordination environment across multiple analogue systems. This is the case for $[Ho(\beta_2\text{-}SiW_{11}O_{39})_2]^{13-}$, $[Ho(\beta\text{-}Mo_8O_{26})_2]^{5-}$ and $[Ho\{Mo_5O_{13}(OMe)_4NNC_6H_4\text{-}p\text{-}NO_2\}_2]^{3-}$.[26,48] Just like $Na_9[Ho(W_5O_{18})_2]\cdot35H_2O$, these systems host near-D_{4d} environments and a tunnel-split $M_J = \pm4$ ground state. They are also theoretically predicted to display atomic clock transitions, but with different crystal field energy level splitting schemes. In any case, we anticipate that the position of the M_J levels will be less sensitive to isotopic substitution, pressure, or strain.

Regarding decoherence pathways in $Na_9[Ho_xY_{(1-x)}(W_5O_{18})_2]\cdot35H_2O$, our analysis supports a qualitative understanding of the strongly temperature-dependent coherence time T_2 at the atomic clock transitions. T_2 is experimentally determined to be T_1-limited up to concentrations of $x = 0.01$ and down to temperatures of 5 K.[11] In the present work, we demonstrate that there is a relatively dense population of energy levels - both crystal field and vibrational - in the region near 100 cm^{-1}, and that they engage in significant vibronic coupling. This means that even a small population of these levels at relatively low temperatures is expected to have a significant detrimental effect on coherence. We also explored this issue quantitatively, comparing Orbach processes with local mode relaxation mechanisms based on our calculated normal modes and vibronic couplings (Section S4, Supporting Information). For the local mode relaxation mechanism, we find that the thermal evolution of T_1 is consistent with experimental behavior, with a calculated relaxation rate that is approximately 3 times higher at 7 K compared with that at 5 K (Fig. S11, Supporting Information). In $Na_9[Ho_xY_{(1-x)}(W_5O_{18})_2]\cdot35H_2O$, there is limited frequency overlap between the crystal field levels and the phonon manifold due to the transparency window between 250 and 330 cm^{-1}. Should it be possible to alter the coordination environment to place this large "hole" in the phonon density of states at lower frequencies, it would render many of the vibronic pathways in this system ineffective in terms of generating decoherence. The transparency window in the phonon density of states renders some pathways ineffective even now. A full

separation of the electronic and vibrational excitations is likely to entirely eliminate vibronic coupling as a decoherence mechanism.

Concluding remarks

We combined far infrared spectroscopy and high field techniques with lattice dynamics and vibronic coupling models in order to explore the intersection of charge, structure, and magnetism and gain insight into the T_1 relaxation pathways in $Na_9[Ho(W_5O_{18})_2]\cdot35H_2O$ - a model qubit system with atomic clock transitions. We find strong magneto-infrared effects near 370 and 63 cm^{-1} due to mixing of odd-symmetry vibrations with f-manifold crystal field excitations. Specifically, the $M_J = \pm7$ crystal field levels couple to the various HoO_8 rocking and stretching modes. At the same time, the $M_J = \pm5$ levels near 63 cm^{-1} (and very likely the $M_J = \pm2$ levels) are activated by nearby phonons such as asymmetric HoO_8 stretching with cage tilting. Moreover, we report the first direct evidence for a transparency window in the phonon density of states in a robust clock-like molecular spin qubit. Besides exploring the consequences of this "hole" on vibronic coupling, we use our findings to propose design rules aimed at mitigating thermal decoherence pathways involving vibronic coupling. In addition to isotope effects and studies of chemically analogous Ho-containing polyoxometalates, we discuss specific suggestions for alternate rare earth ions and coordination effects as well as stiffer surrounding ligands. Both the site-specific spectroscopic techniques and the first principles theoretical approaches demonstrated herein can be applied to determine phonons as well as the hierarchy of the crystal field energy levels in other f-block complexes, regardless of the coordination environment. This approach has the potential to accelerate the development of molecular spin qubits with improved lifetimes and higher operating temperatures.

Methods

Crystal growth and sample preparation: Single crystals of $Na_9[Ho(W_5O_{18})_2] \cdot 35H_2O$ were grown by solution techniques.[11] The non-magnetic Y^{3+} analog was prepared as well. In order to control the optical density, we combined the single crystals with paraffin (which is transparent in the far infrared region) to create polycrystalline $Na_9[Ho(W_5O_{18})_2] \cdot 35H_2O$ pellets with suitable optical density.

Far infrared spectroscopy: We employed a Bruker 113v Fourier transform infrared spectrometer equipped with a bolometer detector to reveal the far infrared response of $Na_9[Ho(W_5O_{18})_2] \cdot 35H_2O$. The measured transmittance $T(\omega)$ was converted to absorption as $\alpha(\omega) = -\frac{1}{hd} \ln(T(\omega))$. Here, h is the loading, and d is the thickness. An open flow cryostat was used for temperature control. Magneto-infrared work was performed at the National High Magnetic Field Laboratory in Tallahassee, FL using a Bruker 66V/S spectrometer and a 35 T resistive magnet. Absorption differences are ideal for revealing small field-induced spectral changes. They are calculated as: $\Delta\alpha(\omega, H) = \alpha(\omega, H) - \alpha(\omega, H = 0 \text{ T})$. Here, H is applied magnetic field, and ω is the frequency. Stability tests, based upon zero/zero spectra give ane RMS noise level in the magneto-infrared measurements of approximately 0.2%.

DFT calculations: The structural optimization of the crystallographic coordinates (in vacuum) and the vibrational modes calculations were carried out at DFT level using the Gaussian16 package in its revision A.03.[49] Vibrational frequency calculations were performed using both the fully optimized structure and the X-ray crystal structure with no optimization. The PBE0 hybrid exchange-correlation functional was used for both optimization and frequency calculations in combination with Stuttgart RSC ANO basis set with effective core potential (ECP) for the Ho^{3+} cation. CRENBL basis set have been used for W with corresponding ECP potential and 6-31G(d,p) basis set had been used for oxygen. An 'ultra-fine' integration grid and 'very tight' SCF convergence criterion were applied. Dispersion effects

were taken into account using the empirical GD3BJ dispersion correction.

***Ab initio* calculations:** The time-independent electronic structure was computed using the multireference Complete Active Self-Consistent Field Spin-Orbit (CASSCF-SO) method as implemented in the OpenMOLCAS program package (version 18.09).[50] The molecular geometry was extracted from the crystal structure determined by Single Crystal X-ray diffraction and was fully optimized at density functional theory (DFT) level (*vide infra*). In addition, the electronic structure of the molecular geometry with no prior optimization was calculated. Scalar relativistic effects were taken into account with the Douglas–Kroll–Hess transformation using the relativistically contracted atomic natural orbital ANO-RCC basis set with VDZP quality for all atoms. The active space consisted of 10 electrons on the 7 f-orbitals of Ho^{3+} ion. The molecular orbitals were optimized at the CASSCF level in a state-average (SA) over 35 quintets of the ground state term ($L = 6$ for Ho^{3+}). The wave functions obtained at CASSCF were then mixed by spin-orbit coupling by means of the RASSI approach. The combined effect of the crystal field and the spin orbit coupling were computed using SINGLE-ANISO module.[51]

Vibronic coupling: For vibronic-coupling-dependent infrared absorption spectra, we defined an effective Hamiltonian described as:

$$\hat{H}_{eff} = \hat{H}_S \otimes \mathbb{I}_{vib} + \mathbb{I}_S \otimes \hat{H}_{vib} + \hat{H}_{S-vib} \tag{1}$$

where $\hat{H}_S$, $\hat{H}_{vib}$ and $\hat{H}_{S-vib}$ correspond to the system, the vibration (bath) and the spin-vibration Hamiltonian, which can be written as:

$$\hat{H}_S = \sum_{k=2,4,6} \sum_{q=-k}^{k} B_k^q \hat{O}_k^q(J) \tag{2}$$

$$\hat{H}_{vib} = \sum_{j} \hbar\omega_j(n_j + 1/2) \tag{3}$$

$$\hat{H}_{S-vib} = \sum_j \sum_{kq} \hat{Q}_j \left(\frac{\partial B_k^q}{\partial Q_j} \right)_0 \hat{O}_k^q(J) \tag{4}$$

where B_k^q and $\hat{O}_k^q(J)$ correspond to the crystal field parameter and the Stevens operator, respectively. j is an index running over the vibrations and n_j correspond to the vibrational level of mode j. $\hat{Q}_j$ denotes the vibrational coordinate and the term $\left(\frac{\partial B_k^q}{\partial Q_j} \right)_0$ is the vibronic coupling for a given vibrational mode j. To compute this term, we carried out *ab initio* calculations at CASSCF-SO level. The introduction of vibronic coupling is key to compute the infrared absorption spectra, since due to the mixing more transitions will be optically allowed. Complete details can be found in the Supporting Information Section S3.

Acknowledgements

Supporting Information

Detailed explanation of the mode assignments, variable temperature response, spectroscopic methods and theoretical calculations.

References

(1) Coronado, E. Molecular magnetism: from chemical design to spin control in molecules, materials and devices. *Nature Reviews Materials* **2020**, *5*, 87–104.

(2) Gaita-Ariño, A.; Luis, F.; Hill, S.; Coronado, E. Molecular spins for quantum computation. *Nature Chemistry* **2019**, *11*, 301–309.

(3) Atzori, M.; Sessoli, R. The second quantum revolution: role and challenges of molecular chemistry. *Journal of the American Chemical Society* **2019**, *141*, 11339–11352.

(4) Woodruff, D. N.; Winpenny, R. E.; Layfield, R. A. Lanthanide single-molecule magnets. *Chemical Reviews* **2013**, *113*, 5110–5148.

(5) McAdams, S. G.; Ariciu, A.-M.; Kostopoulos, A. K.; Walsh, J. P.; Tuna, F. Molecular single-ion magnets based on lanthanides and actinides: Design considerations and new advances in the context of quantum technologies. *Coordination Chemistry Reviews* **2017**, *346*, 216–239.

(6) Aromí, G.; Roubeau, O. *Handbook on the Physics and Chemistry of Rare Earths*; Elsevier, 2019; Vol. 56; pp 1–54.

(7) Guo, F.-S.; Day, B. M.; Chen, Y.-C.; Tong, M.-L.; Mansikkamäki, A.; Layfield, R. A. Magnetic hysteresis up to 80 kelvin in a dysprosium metallocene single-molecule magnet. *Science* **2018**, *362*, 1400–1403.

(8) Zadrozny, J. M.; Niklas, J.; Poluektov, O. G.; Freedman, D. E. Millisecond coherence time in a tunable molecular electronic spin qubit. *ACS Central Science* **2015**, *1*, 488–492.

(9) Atzori, M.; Tesi, L.; Morra, E.; Chiesa, M.; Sorace, L.; Sessoli, R. Room-temperature quantum coherence and rabi oscillations in vanadyl phthalocyanine: toward multifunc-

tional molecular spin qubits. *Journal of the American Chemical Society* **2016**, *138*, 2154–2157.

(10) Bader, K.; Dengler, D.; Lenz, S.; Endeward, B.; Jiang, S.-D.; Neugebauer, P.; Van Slageren, J. Room temperature quantum coherence in a potential molecular qubit. *Nature Communications* **2014**, *5*, 1–5.

(11) Shiddiq, M.; Komijani, D.; Duan, Y.; Gaita-Ariño, A.; Coronado, E.; Hill, S. Enhancing coherence in molecular spin qubits via atomic clock transitions. *Nature* **2016**, *531*, 348–351.

(12) Hackermüller, L.; Hornberger, K.; Brezger, B.; Zeilinger, A.; Arndt, M. Decoherence of matter waves by thermal emission of radiation. *Nature* **2004**, *427*, 711–714.

(13) Chirolli, L.; Burkard, G. Decoherence in solid-state qubits. *Advances in Physics* **2008**, *57*, 225–285.

(14) Graham, M. J.; Zadrozny, J. M.; Shiddiq, M.; Anderson, J. S.; Fataftah, M. S.; Hill, S.; Freedman, D. E. Influence of electronic spin and spin–orbit coupling on decoherence in mononuclear transition metal complexes. *Journal of the American Chemical Society* **2014**, *136*, 7623–7626.

(15) Goodwin, C. A.; Reta, D.; Ortu, F.; Chilton, N. F.; Mills, D. P. Synthesis and electronic structures of heavy lanthanide metallocenium cations. *Journal of the American Chemical Society* **2017**, *139*, 18714–18724.

(16) Tarantul, A.; Tsukerblat, B. Magnetic relaxation in V15 cluster: Direct spin-phonon transitions. *Inorganica Chimica Acta* **2010**, *363*, 4361–4367.

(17) Tarantul, A.; Tsukerblat, B. Direct and two-phonon Orbach-Aminov type spin-lattice relaxation in molecular magnet V15. Journal of Physics: Conference Series. 2011; p 012007.

(18) Shiozaki, R.; Inagaki, A.; Nishino, A.; Nishio, E.; Maekawa, M.; Kominami, H.; Kera, Y. Spectroscopic investigation of a series of sodium lanthanide decatungstates, $Na_7H_2Ln(III)(W_5O_{18})_2 \cdot nH_2O$ (Ln: La-Yb): the contribution of $4f^n$ electrons to bonding interaction among Ln(III) and polyoxotungstates. *Journal of Alloys and Compounds* **1996**, *234*, 193–198.

(19) AlDamen, M. A.; Cardona-Serra, S.; Clemente-Juan, J. M.; Coronado, E.; Gaita-Ariño, A.; Martí-Gastaldo, C.; Luis, F.; Montero, O. Mononuclear lanthanide single molecule magnets based on the polyoxometalates $[Ln(W_5O_{18})_2]^{9-}$ and $[Ln(\beta_2\text{-}SiW_{11}O_{39})_2]^{13-}$ (Ln^{III} = Tb, Dy, Ho, Er, Tm, and Yb). *Inorganic Chemistry* **2009**, *48*, 3467–3479.

(20) Gu, Y.-N.; Chen, Y.; Wu, Y.-L.; Zheng, S.-T.; Li, X.-X. A series of banana-shaped 3d-4f heterometallic cluster substituted polyoxometalates: syntheses, crystal structures, and magnetic properties. *Inorganic Chemistry* **2018**, *57*, 2472–2479.

(21) AlDamen, M. A.; Clemente-Juan, J. M.; Coronado, E.; Martí-Gastaldo, C.; Gaita-Ariño, A. Mononuclear lanthanide single-molecule magnets based on polyoxometalates. *Journal of the American Chemical Society* **2008**, *130*, 8874–8875.

(22) Li, D.; Parkin, S.; Wang, G.; Yee, G. T.; Clérac, R.; Wernsdorfer, W.; Holmes, S. M. An $S = 6$ cyanide-bridged octanuclear $Fe^{III}_4Ni^{II}_4$ complex that exhibits slow relaxation of the magnetization. *Journal of the American Chemical Society* **2006**, *128*, 4214–4215.

(23) Ghosh, S.; Datta, S.; Friend, L.; Cardona-Serra, S.; Gaita-Ariño, A.; Coronado, E.; Hill, S. Multi-frequency EPR studies of a mononuclear holmium single-molecule magnet based on the polyoxometalate $[Ho^{III}(W_5O_{18})_2]^{9-}$. *Dalton Transactions* **2012**, *41*, 13697–13704.

(24) Liu, J.; Mrozek, J.; Duan, Y.; Ullah, A.; Baldoví, J. J.; Coronado, E.; Gaita-Ariño, A.;

21

Ardavan, A. Quantum coherent spin-electric control in molecular nanomagnets. *arXiv preprint arXiv:2005.01029* **2020**,

(25) Vonci, M.; Giansiracusa, M. J.; Van den Heuvel, W.; Gable, R. W.; Moubaraki, B.; Murray, K. S.; Yu, D.; Mole, R. A.; Soncini, A.; Boskovic, C. Magnetic excitations in polyoxotungstate-supported lanthanoid single-molecule magnets: an inelastic neutron scattering and ab initio study. *Inorganic Chemistry* **2017**, *56*, 378–394.

(26) Baldoví, J. J.; Clemente-Juan, J. M.; Coronado, E.; Duan, Y.; Gaita-Ariño, A.; Giménez-Saiz, Construction of a general library for the rational design of nanomagnets and spin qubits based on mononuclear f-block complexes. The polyoxometalate case. *Inorganic Chemistry* **2014**, *53*, 9976–9980.

(27) Brinzari, T.; Chen, P.; Sun, Q.-C.; Liu, J.; Tung, L.-C.; Wang, Y.; Schlueter, J.; Singleton, J.; Manson, J. L.; Whangbo, M.-H., et al. Quantum critical transition amplifies magnetoelastic coupling in $Mn[N(CN)_2]_2$. *Physical Review Letters* **2013**, *110*, 237202.

(28) Brinzari, T. V.; Haraldsen, J. T.; Chen, P.; Sun, Q.-C.; Kim, Y.; Tung, L.-C.; Litvinchuk, A. P.; Schlueter, J. A.; Smirnov, D.; Manson, J. L., et al. Electron-phonon and magnetoelastic interactions in ferromagnetic $Co[N(CN)_2]_2$. *Physical Review Letters* **2013**, *111*, 047202.

(29) Härtle, R.; Butzin, M.; Rubio-Pons, O.; Thoss, M. Quantum interference and decoherence in single-molecule junctions: how vibrations induce electrical current. *Physical Review Letters* **2011**, *107*, 046802.

(30) Ballmann, S.; Härtle, R.; Coto, P. B.; Elbing, M.; Mayor, M.; Bryce, M. R.; Thoss, M.; Weber, H. B. Experimental evidence for quantum interference and vibrationally induced decoherence in single-molecule junctions. *Physical Review Letters* **2012**, *109*, 056801.

(31) Escalera-Moreno, L.; Baldoví, J. J.; Gaita-Ariño, A.; Coronado, E. Spin states, vi-

brations and spin relaxation in molecular nanomagnets and spin qubits: a critical perspective. *Chemical Science* **2018**, *9*, 3265–3275.

(32) Ullah, A.; Cerdá, J.; Baldoví, J. J.; Varganov, S. A.; Aragó, J.; Gaita-Ariño, A. In silico molecular engineering of dysprosocenium-based complexes to decouple spin energy levels from molecular vibrations. *The Journal of Physical Chemistry Letters* **2019**, *10*, 7678–7683.

(33) Garlatti, E.; Tesi, L.; Lunghi, A.; Atzori, M.; Voneshen, D.; Santini, P.; Sanvito, S.; Guidi, T.; Sessoli, R.; Carretta, S. Unveiling phonons in a molecular qubit with four-dimensional inelastic neutron scattering and density functional theory. *Nature Communications* **2020**, *11*, 1–10.

(34) Yu, C.-J.; Von Kugelgen, S.; Krzyaniak, M. D.; Ji, W.; Dichtel, W. R.; Wasielewski, M. R.; Freedman, D. E. Spin and Phonon Design in Modular Arrays of Molecular Qubits. *Chemistry of Materials* **2020**, *32*, 10200–10206.

(35) Dominguez-Vidal, A.; Kaun, N.; Ayora-Cañada, M. J.; Lendl, B. Probing intermolecular interactions in water/ionic liquid mixtures by far-infrared spectroscopy. *The Journal of Physical Chemistry B* **2007**, *111*, 4446–4452.

(36) Cole, W. T.; Fellers, R. S.; Viant, M. R.; Leforestier, C.; Saykally, R. J. Far-infrared VRT spectroscopy of the water dimer: characterization of the 20 μ m out-of-plane librational vibration. *The Journal of Chemical Physics* **2015**, *143*, 154306.

(37) Marx, R.; Moro, F.; Dörfel, M.; Ungur, L.; Waters, M.; Jiang, S.-D.; Orlita, M.; Taylor, J.; Frey, W.; Chibotaru, L., et al. Spectroscopic determination of crystal field splittings in lanthanide double deckers. *Chemical Science* **2014**, *5*, 3287–3293.

(38) Kumar, C.; Xiao, Y.; Nair, H.; Voigt, J.; Schmitz, B.; Chatterji, T.; Jalarvo, N.; Brückel, T. Hyperfine and crystal field interactions in multiferroic $HoCrO_3$. *Journal of Physics: Condensed Matter* **2016**, *28*, 476001.

(39) Ungur, L.; Chibotaru, L. F. Ab initio crystal field for lanthanides. *Chemistry–A European Journal* **2017**, *23*, 3708–3718.

(40) Newman, D. J. Theory of lanthanide crystal fields. *Advances in Physics* **1971**, *20*, 197–256.

(41) Hallmen, P. P.; Rauhut, G.; Stoll, H.; Mitrushchenkov, A.; van Slageren, J. Crystal Field Splittings in Lanthanide Complexes: Inclusion of Correlation Effects beyond Second Order Perturbation Theory. *Journal of chemical theory and computation* **2018**, *14*, 3998–4009.

(42) Jones, B.; Varughese, P.; Olejniczak, I.; Pigos, J.; Musfeldt, J.; Landee, C.; Turnbull, M.; Carr, G. Vibrational properties of the one-dimensional, S=1/2, Heisenberg antiferromagnet copper pyrazine dinitrate. *Chemistry of Materials* **2001**, *13*, 2127–2134.

(43) Casto, L.; Clune, A.; Yokosuk, M.; Musfeldt, J.; Williams, T.; Zhuang, H.; Lin, M.-W.; Xiao, K.; Hennig, R.; Sales, B., et al. Strong spin-lattice coupling in $CrSiTe_3$. *APL Materials* **2015**, *3*, 041515.

(44) Sethi, A.; Slimak, J.; Kolodiazhnyi, T.; Cooper, S. Emergent vibronic excitations in the magnetodielectric regime of Ce_2O_3. *Physical Review Letters* **2019**, *122*, 177601.

(45) Tang, F.; Su, Z.; Lao, X.; Bao, Y.; Zhu, D.; Xu, S. The key roles of 4f-level splitting and vibronic coupling in the high-efficiency luminescence of Ce^{3+} ion in LuAG transparent ceramic phosphors. *Journal of Luminescence* **2020**, 117360.

(46) Ishikawa, N.; Sugita, M.; Ishikawa, T.; Koshihara, S.-y.; Kaizu, Y. Lanthanide double-decker complexes functioning as magnets at the single-molecular level. *Journal of the American Chemical Society* **2003**, *125*, 8694–8695.

(47) Escalera-Moreno, L.; Baldoví, J. J.; Gaita-Ariño, A.; Coronado, E. Design of high-temperature f-block molecular nanomagnets through the control of vibration-induced spin relaxation. *Chemical Science* **2020**, *11*, 1593–1598.

(48) Baldoví, J. J.; Duan, Y.; Bustos, C.; Cardona-Serra, S.; Gouzerh, P.; Villanneau, R.; Gontard, G.; Clemente-Juan, J. M.; Gaita-Ariño, A.; Giménez-Saiz, C., et al. Single ion magnets based on lanthanoid polyoxomolybdate complexes. *Dalton Transactions* **2016**, *45*, 16653–16660.

(49) Frisch, M. J., et al. Gaussian 16 Revision A.03. *Gaussian 16 Revision A.03* **2016**,

(50) Fdez. Galvan, I.; Vacher, M.; Alavi, A.; Angeli, C.; Aquilante, F.; Autschbach, J.; Bao, J. J.; Bokarev, S. I.; Bogdanov, N. A.; Carlson, R. K., et al. OpenMolcas: From source code to insight. *Journal of Chemical Theory and Computation* **2019**, *15*, 5925–5964.

(51) Ungur, L.; Chibotaru, L. F. Ab initio crystal field for lanthanides. *Chemistry–A European Journal* **2017**, *23*, 3708–3718.
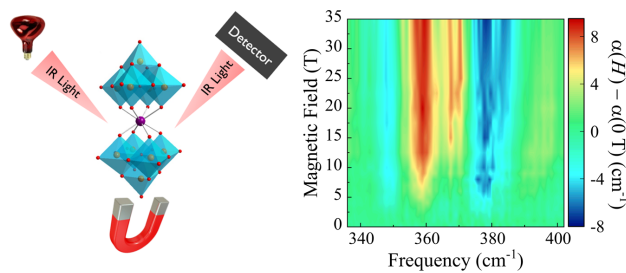
Figure 7: For Table of Contents Only

Vibronic coupling in single molecule magnet, $Na_9[Ho(W_5O_{18})_2] \cdot 35H_2O$, leads to changes in magneto-infrared spectra at high magnetic field.